Chiral bands for a quasi-proton and quasi-neutron coupled with a triaxial rotor

S. Q. Zhang,[1,2,*] B. Qi,[1] S. Y. Wang,[1] and J. Meng[1,2,3,†]

[1]*School of Physics and MOE Key Laboratory of Heavy Ion Physics, Peking University, Beijing 100871, People's Republic of China*

[2]*Institute of Theoretical Physics, Chinese Academy of Sciences, Beijing, 100080, People's Republic of China*

[3]*Center of Theoretical Nuclear Physics, National Laboratory of Heavy Ion Accelerator, Lanzhou 730000, People's Republic of China*

(Received 25 January 2007; published 18 April 2007)

A particle rotor model (PRM) with a quasi-proton and a quasi-neutron coupled with a triaxial rotor is developed and applied to study chiral doublet bands with configurations of an $h_{11/2}$ proton and an $h_{11/2}$ quasi-neutron. With pairing treated by the BCS approximation, the present quasiparticle PRM is aimed at simulating one proton and many neutron holes coupled with a triaxial rotor. After a detailed analysis of the angular momentum orientations, energy separation between the partner bands, and behavior of electromagnetic transitions, for the first time we find aplanar rotation or equivalently chiral geometry beyond the usual one proton and one neutron hole coupled with a triaxial rotor.

DOI: 10.1103/PhysRevC.75.044307 PACS number(s): 21.60.Ev, 21.10.Re, 23.20.Lv

I. INTRODUCTION

Since the pioneering work of Frauendorf and Meng [1], the phenomenon of chiral rotation in atomic nuclei has attracted significant attention. Chirality in nuclei offers direct evidence for the existence of stable triaxial nuclear shapes, in which there are a few high-j valence particles and a few high-j valence holes. For a triaxially deformed rotational nucleus, the collective angular momentum favors alignment along the intermediate axis, which in this case has the largest moment of inertia, whereas the angular momentum vectors of the valence particles (holes) favor alignment along the nuclear short (long) axis. The three mutually perpendicular angular momenta can be arranged to form two systems with opposite chirality, namely left- and right-handedness. They are transformed into each other by the chiral operator that combines time reversal and spatial rotation of 180°, $\chi = \mathcal{TR}(\pi)$. The spontaneous breaking of chiral symmetry thus happens in the body-fixed reference frame. In the laboratory reference frame, with the restoration of chiral symmetry resulting from quantum tunneling, the so-called chiral doublet bands, a pair of separated $\Delta I = 1$ bands (normally regarded as nearly degenerate) with the same parity, are expected to be observed in triaxial nuclei.

Originally the pair of $\Delta I = 1$ bands found in ^{134}Pr with the $\pi h_{11/2} \otimes \nu h_{11/2}$ configuration [2] was reinterpreted in Ref. [1] as a candidate for chiral doubling. Thereafter, similar low-lying doublet bands were reported in $_{55}$Cs, $_{57}$La, and $_{61}$Pm $N = 75$ isotones of ^{134}Pr, and an island of chiral rotation was suggested in the $A \sim 130$ mass region [3]. So far, candidate chiral doublet bands have been proposed in a number of odd-odd nuclei in the $A \sim 130$ [3–12] and $A \sim 100$ mass regions [13–15]. A few more candidates with more than one valence particle and hole were also reported in odd-A [16–19] and even-even nuclei [20].

On the theoretical side, chiral bands were first predicted in the particle rotor model (PRM) and tilted axis cranking (TAC) approach for triaxially deformed nuclei [1]. Numerous efforts have been devoted to the development of the PRM and TAC approaches. Chiral rotation has been studied by the Strutinsky shell correction TAC (SCTAC) method with a hybrid potential that combines the spherical Woods-Saxon single-particle energies and the deformed part of the Nilsson potential [21,22]. Recently, chiral TAC solutions have also been found in $N = 75$ isotones within the self-consistent Skyrme Hartree-Fock cranking model [23,24]. Cranked relativistic mean-field (RMF) theory has been applied only in the contexts of principle axis rotation [25,26] and planar rotation [27]. The generalization thereof for searching for chiral solutions (i.e., the aplanar rotation) is still under development. In Ref. [28], the adiabatic and configuration-fixed constrained triaxial RMF approaches were developed to obtain the nuclear potential energy surface with the triaxial degree of freedom, and the existence of multiple chiral doublets (MχD) was predicted for the $A \sim 100$ mass region based on their triaxial deformations and their corresponding proton and neutron configurations. The advantage of the cranked mean-field approach to describe nuclear rotation bands is that it can be easily extended to the multi-quasiparticle case. However, the usual cranking approach is a semiclassical model, where the total angular momentum is not a good quantum number, and the description of quantum tunneling of chiral partners is beyond the mean-field approximation [28–30].

In contrast, the PRM is a quantum-mechanical model where total angular momentum is a good quantum number. The model describes the system in the laboratory reference frame and yields directly the energy splitting and tunneling between doublet bands. Chirality for nuclei in $A \sim 100$ and $A \sim 130$ regions has been studied with the PRM for certain particle-hole configurations [30,31], or the core-quasiparticle/core-particle-hole coupling model [9,32] following the Kerman-Klein-Dönau-Frauendorf method [33]. Selection rules of electromagnetic transitions for chiral doublet bands have been proposed based on a simple particle-hole-triaxial rotor model [34].

*Electronic address: sqzhang@pku.edu.cn

†Electronic address: mengj@pku.edu.cn

Though various versions of PRM and TAC have been applied to study chiral bands, the essential starting point for understanding their properties is based on one particle and one hole coupled with a rigid triaxial rotor. Based on this scenario, a set of observable signatures has been suggested as fingerprints of chiral bands [1,13,35–37]. Critical analyses for the representative cases of candidate chiral bands, ^{134}Pr in $A \sim 130$ [36] and ^{104,106}Rh in $A \sim 100$ [37], have been carried out. It has been found that these candidate chiral bands in ^{134}Pr and ^{104}Rh do not agree with all of those expected for chiral bands, although these candidates have been considered as the best examples of chiral rotation in the $A \sim 130$ and $A \sim 100$ mass regions (owing to their extremely small level discrepancy between the doublet bands). Lifetime measurements are essential for extracting the absolute $B(M1)$ and $B(E2)$ transition probabilities, which are critical experimental observables in addition to the level energies. Indeed, this has stimulated experimental programs aimed at identifying chiral doublet bands [38,39].

Nevertheless, one should bear in mind that these fingerprints of chiral bands are obtained mostly by assuming one proton (neutron) particle and one neutron (proton) hole sitting in a high-j shell coupled with a triaxial rotor with $\gamma = 30^\circ$. In a realistic nucleus, it is more natural that there will be more than one nucleon in a high-j shell [e.g., the candidate chiral doublet bands reported for $N = 75$ isotones with $Z = 55$ (^{130}Cs), 57(^{132}La), 59(^{134}Pr), 61(^{136}Pm), and 63(^{138}Eu) and for $Z = 55$ (Cs) isotopes with $N = 69, 71, 73, 75$, and 77]. The Fermi energy of a proton (neutron) will undoubtedly change with Z (N) in these isotones (isotopes). Therefore it is interesting and necessary to investigate the doublet bands with valence nucleons sitting in the middle of a high-j shell, or alternatively multi-particles sitting in a high-j shell. It is also important to investigate the properties of doublet bands as functions of the triaxial deformation degree of freedom.

To address these issues, in this paper a PRM with a quasi-proton and a quasi-neutron coupled with a triaxial rotor is developed and applied to study chiral doublet bands with configurations of an $h_{11/2}$ proton and an $h_{11/2}$ quasi-neutron. With the pairing correlations taken into account by the BCS approximation, the configuration of multi-particles sitting in a high-j shell can be simulated by adjusting the neutron Fermi energy. Note that, in a former paper [40], the present model has been applied to the doublet bands of ^{126}Cs, and good agreement with the data available was obtained, which supports the chiral interpretation of these doublet bands. Here the formalism is given in detail and the properties of the doublet bands calculated are presented. The model is introduced in Sec. II. The properties of the doublet bands thus obtained, such as energy spectra, electromagnetic transitions, and the orientation of angular momenta, are discussed in Sec. III. Finally, a summary and conclusion are given in Sec. IV.

II. FORMALISM

The particle rotor model [41] for the triaxial deformed case has been well used for the description of odd-A and odd-odd nuclei [30,42–45]. Its Hamiltonian for an odd-odd nucleus can be expressed as

$$H = H_{\rm coll} + H^p_{\rm intr} + H^n_{\rm intr}, \tag{1}$$

where p and n refer to protons and neutrons, respectively. The collective Hamiltonian takes the form

$$H_{\rm coll} = \sum_{i=1}^{3} \frac{\hat{R}_i^2}{2\mathcal{J}_i} = \sum_{i=1}^{3} \frac{(\hat{I}_i - \hat{j}_{pi} - \hat{j}_{ni})^2}{2\mathcal{J}_i}, \tag{2}$$

where $\hat{R}_i$, $\hat{I}_i$, $\hat{j}_{pi}$, and $\hat{j}_{ni}$, respectively, denote the angular momentum operators for the core and nucleus as well as for the valence proton and neutron. The moments of inertia for irrotational flow are adopted [i.e., $\mathcal{J}_i = \mathcal{J}\sin^2(\gamma - 2\pi i/3)$].

The intrinsic Hamiltonian for valence nucleons is

$$\begin{aligned} H^{p(n)}_{\rm intr} &= H_{\rm sp} + H_{\rm pair} = \sum_{\nu>0}(\varepsilon_\nu - \lambda)(a^+_\nu a_\nu + a^+_{\bar\nu} a_{\bar\nu}) \\ &\quad - \frac{\Delta}{2}\sum_{\nu>0}(a^+_\nu a^+_{\bar\nu} + a_{\bar\nu} a_\nu), \end{aligned} \tag{3}$$

where λ denotes the Fermi energy, Δ is the pairing gap parameter, and $|\bar\nu\rangle$ is the time-reversal state of $|\nu\rangle$. The single-particle energy ε_ν is obtained by the diagonalization of the Hamiltonian $H_{\rm sp}$. Similar to the approach in Ref. [30], for a single-j shell, one has

$$H_{\rm sp} = \pm\frac{1}{2}C\left\{\cos\gamma\left[j_3^2 - \frac{j(j+1)}{3}\right] + \frac{\sin\gamma}{2\sqrt{3}}(j_+^2 + j_-^2)\right\}, \tag{4}$$

where the plus sign refers to a particle, the minus to a hole, and the coefficient C is proportional to the quadrupole deformation β [30,43]. The single-particle states are thus written as

$$a^+_\nu|0\rangle = \sum_\Omega c^{(\nu)}_\Omega \psi^j_\Omega, \quad a^+_{\bar\nu}|0\rangle = \sum_\Omega (-1)^{j-\Omega} c^{(\nu)}_\Omega \psi^j_{-\Omega}, \tag{5}$$

where Ω is the projection of the single-particle angular momentum $\hat{j}$ along the 3-axis and can be restricted to the values $\ldots, -7/2, -3/2, +1/2, +5/2, \ldots$ because of time-reversal degeneracy [44,45].

To obtain the PRM solutions, the total Hamiltonian (1) must be diagonalized in a complete basis space, which couples the rotation of the inert core with the intrinsic wave functions of valence nucleons. When pairing correlations are neglected, one can construct the so-called strong coupling basis as

$$\begin{aligned} |IMK\nu_p\nu_n\rangle &= \sqrt{\frac{1}{2}}\sqrt{\frac{2I+1}{8\pi^2}}\big[D^I_{M,K} a^+_{\nu_p} a^+_{\nu_n}|0\rangle \\ &\quad + (-1)^{I-K} D^I_{M,-K} a^+_{\bar\nu_p} a^+_{\bar\nu_n}|0\rangle\big] \\ &= \sqrt{\frac{2I+1}{16\pi^2}}\sum_{\Omega_p}\sum_{\Omega_n} c^{(\nu_p)}_{\Omega_p} c^{(\nu_n)}_{\Omega_n}\big[D^I_{M,K}\psi^{j_p}_{\Omega_p}\psi^{j_n}_{\Omega_n} \\ &\quad + (-1)^{I-j_p-j_n} D^I_{M,-K}\psi^{j_p}_{-\Omega_p}\psi^{j_n}_{-\Omega_n}\big] \\ \text{for}\quad K &= \pm1, \pm3, \pm5, \ldots, \end{aligned} \tag{6}$$

$$
\begin{aligned}
|IMK\nu_p\bar{\nu}_n\rangle &= \sqrt{\frac{1}{2}}\sqrt{\frac{2I+1}{8\pi^2}}\left[D^I_{M,K}a^+_{\nu_p}a^+_{\bar{\nu}_n}|0\rangle\right.\\
&\quad \left.+(-1)^{I-K}D^I_{M,-K}a^+_{\bar{\nu}_p}a^+_{\nu_n}|0\rangle\right]\\
&= \sqrt{\frac{2I+1}{16\pi^2}}\sum_{\Omega_p}\sum_{\Omega_n}c^{(\nu_p)}_{\Omega_p}c^{(\nu_n)}_{\Omega_n}(-1)^{j_n-\Omega_n}\\
&\quad \times\left[D^I_{M,K}\psi^{j_p}_{\Omega_p}\psi^{j_n}_{-\Omega_n}+(-1)^{I-j_p-j_n}\right.\\
&\quad \left.\times D^I_{M,-K}\psi^{j_p}_{-\Omega_p}\psi^{j_n}_{\Omega_n}\right]\\
\text{for}\qquad K &= 0,\pm2,\pm4,\ldots. \qquad (7)
\end{aligned}
$$

The values of K are restricted because the basis states are symmetrized under the point group D_2, which leads to $K-\Omega_p-\Omega_n$ in Eq. (6) and $K-\Omega_p+\Omega_n$ in Eq. (7) being an even integer [44]. The matrix elements of Hamiltonian (2) and (4) can be evaluated in the basis (6) and (7), and then diagonalization gives eigenenergies and eigenstates for the PRM Hamiltonian. For a certain spin I, the dimension of the basis space will be $(1/4)(2I+1)(2j_p+1)(2j_n+1)$.

To include pairing effects in the PRM, one should replace the single-particle state $a^+_\nu|0\rangle$ in the basis states (6) and (7) with the BCS quasiparticle state $\alpha^+_\nu|\tilde{0}\rangle$ to obtain a new expansion basis, where $|\tilde{0}\rangle$ is the BCS vacuum state. The quasiparticle operators α^+_ν are given by

$$
\begin{pmatrix}\alpha^+_\nu\\ \alpha_{\bar{\nu}}\end{pmatrix}=\begin{pmatrix}u_\nu & -v_\nu\\ v_\nu & u_\nu\end{pmatrix}\begin{pmatrix}a^+_\nu\\ a_{\bar{\nu}}\end{pmatrix}, \qquad (8)
$$

where $u^2_\nu+v^2_\nu=1$. In this new basis, the wave functions of PRM Hamiltonian are written as

$$
|IM\rangle=\sum_{K,\nu_p,\nu_n}\left(C^{IK}_{\nu_p\nu_n}|IMK\nu_p\nu_n\rangle+C^{IK}_{\nu_p\bar{\nu}_n}|IMK\nu_p\bar{\nu}_n\rangle\right), \qquad (9)
$$

in which ν_p and ν_n represent the quasiparticle states $\alpha^+_{\nu_p}|\tilde{0}\rangle$ and $\alpha^+_{\nu_n}|\tilde{0}\rangle$ instead. Furthermore, single-particle energies ε_ν should be replaced by quasiparticle energies $\varepsilon'_\nu=\sqrt{(\varepsilon_\nu-\lambda)^2+\Delta^2}$. The total Hamiltonian then becomes

$$
\begin{aligned}
H &= H_{\text{coll}}+\sum_{\nu_p}\varepsilon'_{\nu_p}\left(\alpha^+_{\nu_p}\alpha_{\nu_p}+\alpha^+_{\bar{\nu}_p}\alpha_{\bar{\nu}_p}\right)\\
&\quad +\sum_{\nu_n}\varepsilon'_{\nu_n}\left(\alpha^+_{\nu_n}\alpha_{\nu_n}+\alpha^+_{\bar{\nu}_n}\alpha_{\bar{\nu}_n}\right). \qquad (10)
\end{aligned}
$$

To construct the matrix of this Hamiltonian, in comparison with the case excluding pairing, each single-particle matrix element needs to be multiplied by a pairing factor $u_\mu u_\nu+v_\mu v_\nu$ [43,45]. The occupation factor v_ν of the state ν is given by

$$
v^2_\nu=\frac{1}{2}\left[1-\frac{\varepsilon_\nu-\lambda}{\varepsilon'_\nu}\right]. \qquad (11)
$$

The reduced electromagnetic transition probabilities are defined as [41]

$$
B(\sigma\lambda, I\to I')=\sum_{\mu M'}\left|\langle I'M'|\mathscr{M}^\sigma_{\lambda\mu}|IM\rangle\right|^2, \qquad (12)
$$

where σ denotes either E or M for electric and magnetic transitions, respectively, λ is the rank of transition operator, and $\mathscr{M}^\sigma_{\lambda\mu}$ is the electromagnetic transition operator.

For electric quadrupole ($E2$) processes, the corresponding transition operator is generally taken as

$$
\mathscr{M}(E2,\mu)=\int\rho_e(\vec{r})r^2Y_{2\mu}(\theta,\phi)d\tau, \qquad (13)
$$

which is proportional to the electric quadrupole tensor operator $\hat{Q}_{2\mu}$ with a factor $\sqrt{5/16\pi}$. The quadrupole moments in the laboratory frame ($\hat{Q}_{2\mu}$) and the intrinsic system ($\hat{Q}'_{2\mu}$) are connected by the relation

$$
\hat{Q}_{2\mu}=\mathcal{D}^{2*}_{\mu0}\hat{Q}'_{20}+\left(\mathcal{D}^{2*}_{\mu2}+\mathcal{D}^{2*}_{\mu-2}\right)\hat{Q}'_{22}. \qquad (14)
$$

For stretched $E2$ transitions, one has

$$
\begin{aligned}
&B(E2, I\alpha\to I'\alpha)\\
&= \frac{5}{16\pi}Q_0^2\left|\sum_{\nu_p\nu_n}^{KK'}C^{IK}_{\nu_p\nu_n}C^{I'K'}_{\nu_p\nu_n}\left[\langle IK20|I'K'\rangle\cos\gamma\right.\right.\\
&\quad \left.\left.+\frac{\sin\gamma}{\sqrt{2}}(\langle IK22|I'K'\rangle+\langle IK2-2|I'K'\rangle)\right]\right|^2\\
&\quad +\text{Term2}, \qquad (15)
\end{aligned}
$$

where Q_0 is the intrinsic charge quadrupole moment and the "Term2" term is the same as the first term but with the replacement $(\nu_n\to\bar{\nu}_n)$.

For $M1$ transitions, the magnetic dipole transition operator can be written as

$$
\mathscr{M}(M1,\mu)=\sqrt{\frac{3}{4\pi}}\frac{e\hbar}{2Mc}[(g_p-g_R)\hat{j}_{p\mu}+(g_n-g_R)\hat{j}_{n\mu}], \qquad (16)
$$

where g_p, g_n, and g_R are, respectively, the effective gyromagnetic ratios for valence proton, valence neutron, and the collective core, and $\hat{j}_\mu$ denotes the spherical tensor in the laboratory frame. The $M1$ reduced transition probability $B(M1)$ is expressed as

$$
\begin{aligned}
&B(M1, I\alpha\to I'\alpha)\\
&= \frac{3}{4\pi}\left|\sum_{\mu KK'}C^{IK}_{\nu_p\nu_n}C^{I'K'}_{\nu'_p\nu'_n}\sum_{\Omega'_p\Omega'_n}c^{(\nu'_p)}_{\Omega'_p}c^{(\nu'_n)}_{\Omega'_n}\sum_{\Omega_p\Omega_n}c^{(\nu_p)}_{\Omega_p}c^{(\nu_n)}_{\Omega_n}\right.\\
&\quad \times\{\langle IK1\mu|I'K'\rangle\langle\Omega'_p\Omega'_n|\hat{T}_\mu|\Omega_p\Omega_n\rangle+(-1)^{I-j_p-j_n}\\
&\quad \left.\times\langle I-K1\mu|I'K'\rangle\langle\Omega'_p\Omega'_n|\hat{T}_\mu|-\Omega_p-\Omega_n\rangle\}\right|^2\\
&\quad +\text{Term2}+\text{Term3}+\text{Term4}, \qquad (17)
\end{aligned}
$$

where terms "Term2," "Term3," and "Term4" are the same as the first term but with the replacements $(\nu_n\to\bar{\nu}_n)$, $(\nu'_n\to\bar{\nu}'_n)$, and $(\nu_n\to\bar{\nu}_n, \nu'_n\to\bar{\nu}'_n)$, respectively. The operator $\hat{T}_\mu$ in Eq. (17) is given by

$$
\hat{T}_\mu=f(p)(g_p-g_R)\hat{j}_{p\mu}+f(n)(g_n-g_R)\hat{j}_{n\mu}, \qquad (18)
$$

with $f(p)$ and $f(n)$ the pairing factors $uu' + vv'$ for proton and neutron, and j_μ the rank-1 spherical tensor in the body-fixed reference frame.

III. RESULTS AND DISCUSSION

A. Single-particle states in the single-j model

For the intrinsic Hamiltonian of valence nucleons, we apply the simple single-j model, which is a good approximation for high-j intruder orbitals [41]. The single-particle energy ε corresponding to the Hamiltonian in Eq. (4) with a $1h_{11/2}$ j shell and $C = 0.3$ MeV is plotted in the upper panel of Fig. 1 as a function of the γ deformation of the deformed well. This $C = 0.3$ MeV corresponds to a quadrupole deformation of $\beta \sim 0.28$ for the $1h_{11/2}$ subshell in the $A \sim 130$ mass region. When $\gamma = 0^\circ$ (i.e., the axial symmetrical case), there are six discrete states with good quantum number $\Omega(\pm 1/2, \pm 3/2, \ldots, \pm 11/2)$. These states are indexed by $\nu(\nu = 1, 2, \ldots, 6)$, and the corresponding energies are denoted by ε_ν. When axial symmetry is broken, Ω is not a good quantum number, and each single-particle state ν is then a superposition of eigenstates of (j^2, j_3) as in Eq. (5) and changes smoothly with γ. It can be clearly seen that for an $h_{11/2}$ particle, a lower energy is obtained for $\gamma = 60^\circ$ (i.e., an oblate shape is preferred), whereas for a hole a prolate shape is preferred. Particularly, for a nucleus with a $\pi h_{11/2} \otimes \nu h_{11/2}^{-1}$ configuration, the sum of single-particle energies will be fairly γ soft with a minimum around $\gamma = 30^\circ$, and the γ degree of freedom will play an important role. Note that the single-particle energies for levels 2 and 5 are nearly γ independent.

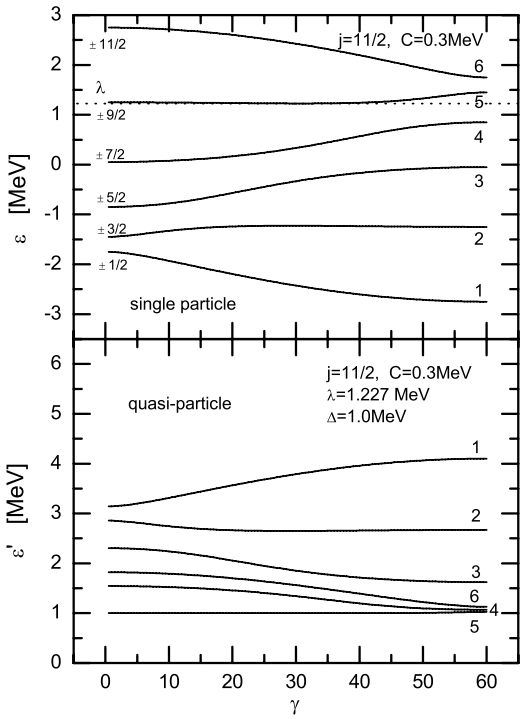

FIG. 1. (Upper panel) The single-particle energy ε with single-j Hamiltonian in Eq. (4) ($j = 11/2$, $C = 0.3$ MeV) as a function of γ deformation. The six degenerate levels are, respectively, indicated by $1, 2, \ldots, 6$ and the corresponding third angular momentum components are $\pm 1/2, \pm 3/2, \ldots, \pm 11/2$ at $\gamma = 0^\circ$ (which is a good quantum number only for $\gamma = 0^\circ$). The dashed line indicates the Fermi energy λ, which is used to obtain the quasiparticle energy ε' in the lower panel. (Lower panel) Quasiparticle energy ε' for the same parameters as a function of γ deformation. The pairing parameters are $\lambda = 1.227$ MeV, $\Delta = 1$ MeV. Each level $(1, 2, \ldots, 6)$ corresponds to that with the same number in the upper panel.

With pairing taken into account by the BCS calculation, the quasiparticle energy ε' with $\lambda = 1.227$ MeV and $\Delta = 1$ MeV is given in the lower panel of Fig. 1. The Fermi energy λ is very close to ε_5, which is shown by a dashed line in the upper panel. The label for each level follows the corresponding one in the upper panel. Since the Fermi energy is $\lambda \approx \varepsilon_5$, the state ε_5 is now the lowest quasiparticle state located at $\sim$1 MeV owing to the pairing gap Δ. Another feature is that the quasiparticle energy ε'_ν becomes more γ soft than the corresponding single-particle energy ε_ν owing to pairing.

B. Energy spectra

In the present PRM, if $\lambda_n = \varepsilon_6$ and $\Delta_n = 0$ for the neutron, and $\lambda_p = \varepsilon_1$ and $\Delta_p = 0$ for the proton, the model discussed here is equivalent to the model in Refs. [1,30,34]. In the following calculation, $\lambda_p = \varepsilon_1$ and $\Delta_p = 0$ are fixed for the proton (i.e., a pure $h_{11/2}$ particle proton), while λ_n for the neutron changes from the bottom to the top of the $h_{11/2}$ shell. The coefficient $C = 0.3$ MeV, which corresponds to a quadrupole deformation of $\beta \sim 0.28$ for the $A \sim 130$ mass region, and the moment of inertia is $\mathcal{J} = 30$ MeV^{-1}. For the electromagnetic transition probabilities, the intrinsic charge quadrupole momentum Q_0 takes a value of $3.5\,e$ b, and the g factors $g_p - g_R = 0.7$ and $g_n - g_R = -0.6$, respectively, are adopted.

First we investigate the behavior of doublet bands for a nucleus at the deformation $\gamma = 30^\circ$ in which the best chirality of nuclear rotation is expected [1]. It should be noted that, for an asymmetric configuration $\pi g_{9/2}^{-1} \otimes \nu h_{11/2}$, the best chirality occurs at a deformation $\gamma = 27^\circ$ in Ref. [30].

The calculated rotational spectra for the yrast and yrare bands[1] with the configuration $\pi h_{11/2} \otimes \nu h_{11/2}$ for $C = 0.3$ MeV and $\mathcal{J} = 30$ MeV^{-1} are plotted in Fig. 2. In the calculations, the odd proton is fixed to be a pure $h_{11/2}$ particle, while the odd neutron is treated as a BCS quasiparticle with $\Delta = 1$ MeV and $\lambda_n = \varepsilon_1, \varepsilon_2, \ldots, \varepsilon_6$, respectively. The $I = 9$ state energies of the yrast bands are taken as reference points and are separated by 2.0 MeV for display. From Fig. 2, the energy difference between the yrare and yrast bands increases from $\lambda_n = \varepsilon_6$ to ε_1. For $\lambda_n = \varepsilon_6$, two nearly degenerate bands can be clearly seen, especially for the spin interval $13 \leqslant I \leqslant 17$, and the energy difference between the doublet

[1]In the paper, the yrast band denotes the rotational band that connects the lowest energies with given spins I obtained from the present PRM calculations, whereas the yrare band correspondingly connects the second lowest energies.

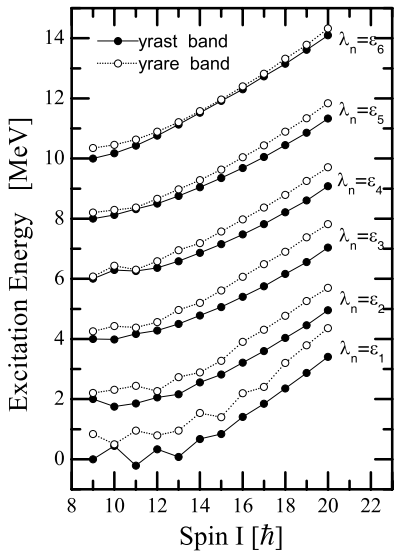

FIG. 2. Calculated rotational spectra for the yrast (solid circles) and yrare (open circles) bands for the configuration $\pi h_{11/2} \otimes \nu h_{11/2}$ with $C = 0.3$ MeV, $\mathcal{J} = 30\,\mathrm{MeV}^{-1}$, and $\gamma = 30^\circ$. In the calculations, the odd proton is fixed to be a pure $h_{11/2}$ particle, whereas the odd neutron is treated as a BCS quasiparticle with $\lambda_n = \varepsilon_1, \varepsilon_2, \ldots, \varepsilon_6$, respectively, and $\Delta = 1$ MeV. The $I = 9$ state energies of the yrast bands, assumed to be 0 MeV, are separated by 2.0 MeV for display.

bands is below 100 keV. This is the classical case where the chiral concept was proposed [1]. When $\lambda_n = \varepsilon_5$, the two bands are nearly degenerate with a constant energy separation of $\sim$200 keV for the spin interval $11 \leqslant I \leqslant 15$ and a gradually increasing energy separation for higher spin. For $\lambda_n = \varepsilon_4$ and ε_3, the spectra present very similar behavior: (1) At the low spin region $I < 14$, a slight odd-even staggering with opposite phase can be seen for yrast and yrare bands; (2) only at low spins ($I = 9, 11, 12$) is the energy difference of the yrast and yrare states smaller than 250 keV; (3) for spin $I \geqslant 14$, the energy differences between yrast and yrare states increase with I (e.g., $\sim$ 400 keV at $I = 14$ and $\sim$ 700 keV at $I = 20$). For $\lambda_n = \varepsilon_1$, odd-even staggering becomes more obvious and the two bands are separated by an average energy of $\sim$800 keV. The case of $\lambda_n = \varepsilon_2$ is in between that of ε_3 and that of ε_1.

The calculated energy difference $E_2(I) - E_1(I)$ between yrare and yrast bands at spins $I = 12, 13, \ldots, 17$ as a function of γ deformation is plotted in Fig. 3. The left panel displays the results for a pure $h_{11/2}$ proton particle and a pure $h_{11/2}$ neutron hole ($\lambda_n = \varepsilon_6$, $\Delta = 0$) configuration. One can see a symmetric $E_2(I) - E_1(I)$ curve about $\gamma = 30^\circ$, which in turn is associated with the symmetries of Hamiltonians with respect to $\gamma = 30^\circ$. If we use $\Delta = 1$ MeV instead for neutrons, the symmetry will not strictly hold any more. In detail, the smallest energy difference (<200 keV) takes place at $\gamma = 30^\circ$ for all the shown spins, and particularly at spins $I = 15, 17$, very good degeneracy is obtained; namely, the energy differences are 7.2 and 4.1 keV, respectively. The energy difference increases when the γ degree deviates from 30°, and it presents a parabola-like curve. At $\gamma = 20^\circ$ and 40°, the value of $E_2(I) - E_1(I)$ varies from 100 to 250 keV, whereas at $\gamma = 15^\circ$ and 45°, the difference is around 450 keV.

In the right panel of Fig. 3, the results for a pure $h_{11/2}$ proton particle and a neutron quasiparticle with $\lambda_n = \varepsilon_5$ and

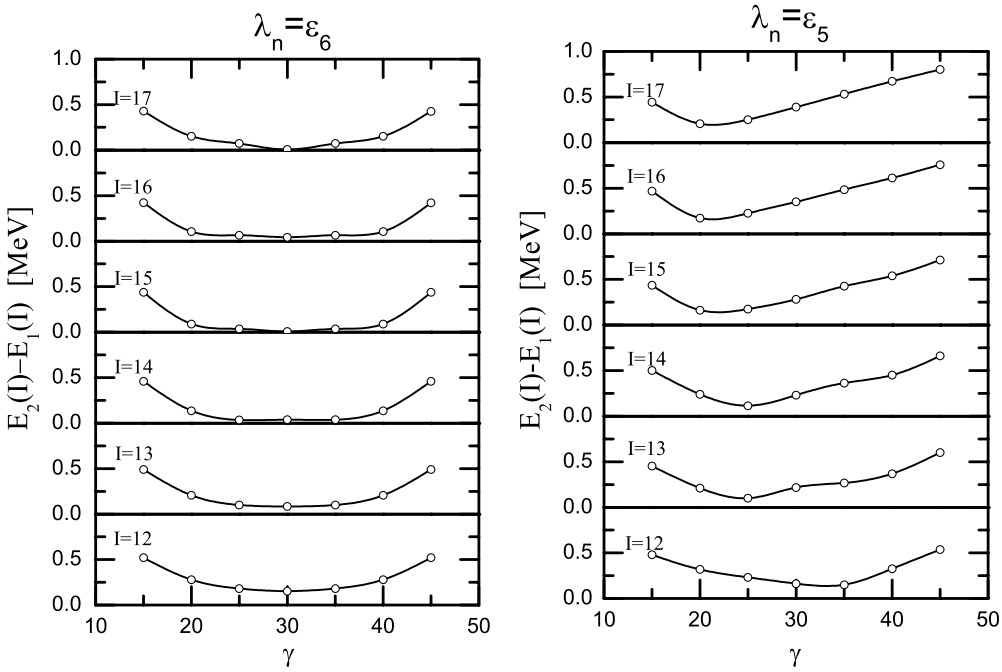

FIG. 3. Calculated energy difference $E_2(I) - E_1(I)$ between yrare and yrast bands at $I = 12, 13, \ldots, 17$ as a function of γ deformation. In the calculations, $C = 0.3$ MeV, $\mathcal{J} = 30\,\mathrm{MeV}^{-1}$, and the odd proton is fixed to be a pure $h_{11/2}$ particle, whereas the odd neutron is treated as a BCS quasiparticle with $\Delta = 1$ MeV and $\lambda_n = \varepsilon_6$ (left panel) or $\lambda_n = \varepsilon_5$ (right panel).

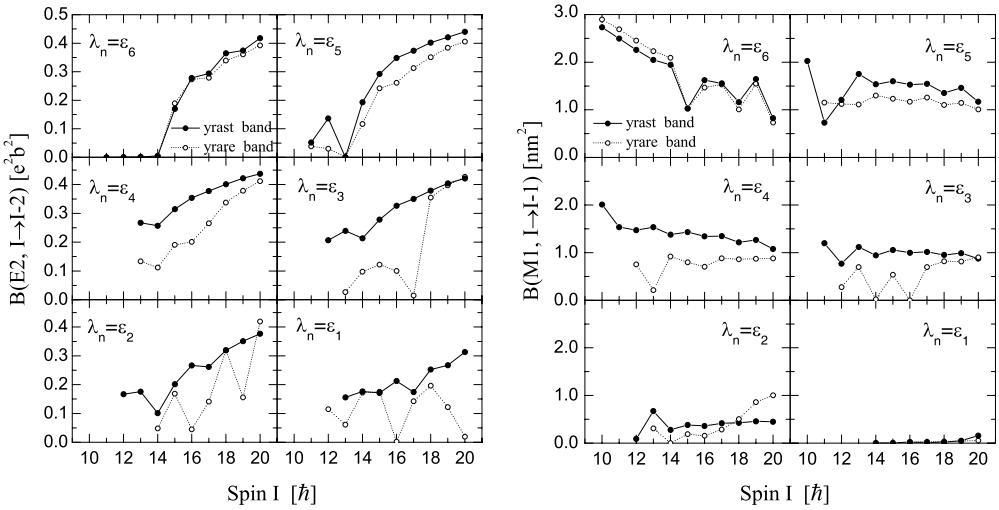

FIG. 4. Calculated $B(E2)$ and $B(M1)$ values for the yrast and yrare bands. The same parameters as Fig. 2 are used.

$\Delta = 1$ MeV are shown. The $E_2(I) - E_1(I)$ curves are still parabola-like, but their minima change with the spin I. The tendency is for the γ deformation with the minimum energy difference to decrease with spin. It is noted that for $\gamma \in (20^\circ, 30^\circ)$, a near-constant energy difference ($\sim$200–250 keV) is observed. Also, the energy difference between the yrast and yrare bands is quite large (exceeding 450 keV) when the nuclear triaxiality is not prominent (i.e., $\gamma \leqslant 15^\circ$ or $\gamma \geqslant 45^\circ$).

Among the candidate chiral doublet bands observed experimentally, there are cases with a degeneracy point (e.g., ^{134}Pr with $\pi h_{11/2} \otimes \nu h_{11/2}$ [36] and ^{104}Rh with $\pi g_{9/2} \otimes \nu h_{11/2}$ [13]) or cases with a near-constant energy difference (e.g., ^{126,128,130,132}Cs [9,12] and ^{106}Rh [14]). Reference [9] suggests that the near-constant energy difference may come from a deviation of the core shape from maximum triaxiality and a less favorable treatment for the valence proton and neutron as a particle-hole configuration. Here our calculations show that either a deviation of the core shape from maximum triaxiality or a deviation of the Fermi energy surface from a particle-hole configuration will hinder the level degeneracy and prefer a near-constant energy difference.

It is also demonstrated that the small energy difference between the doublet bands suggests a triaxiality ($20^\circ < \gamma < 40^\circ$) for the nucleus, in comparison with a difference of more than 450 keV for $\gamma \leqslant 15^\circ$ or $\gamma \geqslant 45^\circ$.

C. Electromagnetic properties

Electromagnetic transition probabilities are critical observables that carry important information on the nuclear intrinsic structure. Using a simple model for a special configuration in triaxial odd-odd nuclei, Koike *et al.* suggested the selection rules for electromagnetic transitions in chiral geometry [34]. The selection rules yield staggering of $B(M1)/B(E2)$ and $B(M1)_{\rm in}/B(M1)_{\rm out}$ values for the partner band as a function of spin I, where $B(M1)_{\rm in}$ and $B(M1)_{\rm out}$ refer to reduced electromagnetic probabilities for intraband and interband $\Delta I = 1$ transitions, respectively. Such staggering behavior has been regarded as a fingerprint for chirality in odd-odd triaxial nuclei and has been extensively used to support the declaration of chiral doublet bands [13]. It is also acknowledged that in ideal chiral doublet bands the electromagnetic transition probabilities must be identical or, in practice, very similar [36]. In the following, the electromagnetic transition probabilities will be investigated with two quasiparticles coupled with the triaxial rotor model to study whether such behavior of the electromagnetic transition probabilities will be influenced by variations in configurations and triaxial deformation.

Figure 4 shows the intraband $B(E2)$ and $B(M1)$ values of yrast and yrare bands for different neutron Fermi energies with $\gamma = 30^\circ$. In the left panel, when $\lambda_n = \varepsilon_6$, the intraband $B(E2)$ values at spins $I \leqslant 14$ are nearly zero. This is because the yrast and yrare bands are displaced in energy for the lower spin region owing to less defined chiral geometry with insufficient collective rotation, and these bands are mainly connected with $M1$ transitions. Note that the interband $B(E2)$ values from yrare band to yrast band are large in this spin region. For spin $I \geqslant 15$, the intraband $B(E2)$ values increase gradually. For $\lambda_n = \varepsilon_5$, the behavior of intraband $B(E2)$ is similar to the case $\lambda_n = \varepsilon_6$, which is small at low spins, then increases with spin. When $\lambda_n = \varepsilon_4$ or ε_3, the intraband $B(E2)$ values of the yrare bands have large differences in comparison with those of the yrast bands. In general, the $B(E2)$ values of the yrast bands are larger than those of the yrare bands, especially for spin $I \leqslant 17$. Their values become close to each other with $I \geqslant 18$, where the collective rotation of the deformed core makes an important contribution to the total spin. For $\lambda_n = \varepsilon_2$ or ε_1, the intraband $B(E2)$ values of the yrast band increase with spin regularly, whereas those of the yrare band exhibit many irregular oscillations.

For the intraband $B(M1)$ in the right panel of Fig. 4, the values of $B(M1)$ systematically reduce as the neutron Fermi energy surface λ_n decreases from ε_6 to ε_1. When $\lambda_n = \varepsilon_1$, the $M1$ transition almost vanishes because both the valence proton and neutron are particle-like and their contribution to the magnetic moment is canceled by similar angular momentum orientations and different g-factor signs. Therefore the rotation

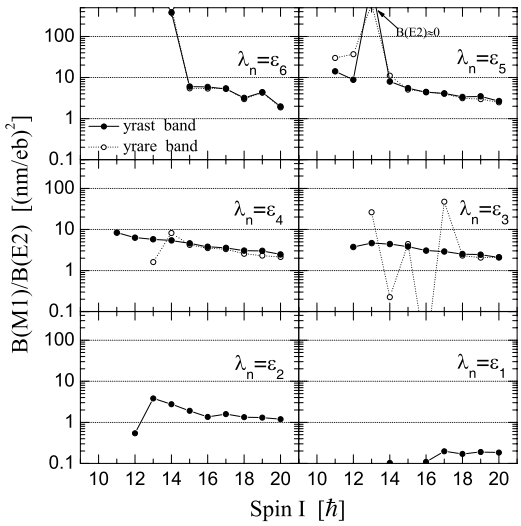

FIG. 5. Calculated $B(M1)/B(E2)$ values for the yrast and yrare bands. The same parameters as Fig. 2 are used.

bands for $\lambda_n = \varepsilon_1$ are mainly connected by $E2$ transitions and correspond to the so-called doubly decoupled bands. For $\lambda_n = \varepsilon_6$ and ε_5, the intraband $B(M1)$ values of yrast and yrare bands are similar to each other. It can also be seen that the odd-even staggering of $B(M1)$ for $\gamma = 30^\circ$ is obvious when $\lambda_n = \varepsilon_6$, but it is not so obvious in other cases.

Figure 5 shows the $B(M1)/B(E2)$ ratios of yrast and yrare bands for different λ_n with $\gamma = 30^\circ$; the ratios of "yrare bands" for $\lambda_n = \varepsilon_2$ and ε_1 are not presented because of their irregular $B(E2)$ values. It is interesting to note that the $B(M1)/B(E2)$ values in partner bands are close to each other for $\lambda_n = \varepsilon_6, \varepsilon_5$, and ε_4, in particular for higher spins, although there are noticeable differences, respectively, in $B(E2)$ and $B(M1)$ values in Fig. 4. Next we examine the odd-even staggering of $B(M1)/B(E2)$ ratios. For $\lambda_n = \varepsilon_6$, staggering can be found for $I > 16$ in the partner bands because of the staggering of $B(M1)$ values. For $\lambda_n = \varepsilon_5$, a delicate staggering for $I > 16$ can be also seen. Except for $I < 18$ in the yrare band for $\lambda_n = \varepsilon_3$, there is no staggering behavior of the $B(M1)/B(E2)$ ratios in the other yrast and yrare bands.

Figure 6 shows the $B(M1)/B(E2)$ values for the yrast and the yrare bands at different γ (i.e., $\gamma = 15^\circ, 20^\circ, 25^\circ, 35^\circ, 40^\circ$, and 45°) with neutron Fermi energy $\lambda_n = \varepsilon_6$ (left panel) and $\lambda_n = \varepsilon_5$ (right panel), respectively. The results with $\gamma = 30^\circ$ have been presented in Fig. 5. One finds that (1) for all γ degrees, the values of $B(M1)/B(E2)$ for the yrast bands are close to those in yrare ones, not only for $\lambda_n = \varepsilon_6$, but also for $\lambda_n = \varepsilon_5$ (three neutron holes approximately); (2) the staggering of $B(M1)/B(E2)$ ratios sensitively depends on the deformation γ.

D. Orientations of angular momenta

The key to the formation of chiral bands in triaxial nuclei is the existence of aplanar total angular momentum. Using wave functions obtained from the PRM, one can calculate the expectation values of angular momenta, $\langle \hat{I}_i \rangle$, $\langle \hat{j}_i \rangle$, and $\langle \hat{R}_i \rangle$. The expectation values for the three components of the angular momenta $\vec{I}$, $\vec{R}$, and $\vec{j}_p$, $\vec{j}_n$ are given as

$$\bar{I}_i \equiv \sqrt{\langle \hat{I}_i^2 \rangle}, \quad \bar{j}_i \equiv \sqrt{\langle \hat{j}_i^2 \rangle}, \quad \bar{R}_i \equiv \sqrt{\langle (\hat{I}_i - \hat{j}_i)^2 \rangle}. \quad (19)$$

In Fig. 7, the average contributions of the three components ${\bar{I}_i}^2/I(I+1)$, $i = 1, 2, 3$, to the total angular momentum, are plotted for the yrast band (left panel) and yrare band (right panel) with λ_n changing from ε_6 to ε_1. In the calculations, $\gamma = 30^\circ$, 1-axis refers to the intermediate axis with the largest moment of inertia, and the 2-axis and 3-axis are, respectively, the short and the long axis with $\mathcal{J}_2 = \mathcal{J}_3 = (1/4)\mathcal{J}_1$. In all panels, it can be seen that the average contributions from I_1 increase globally with the total spin, whereas contributions from the other two directions decrease globally.

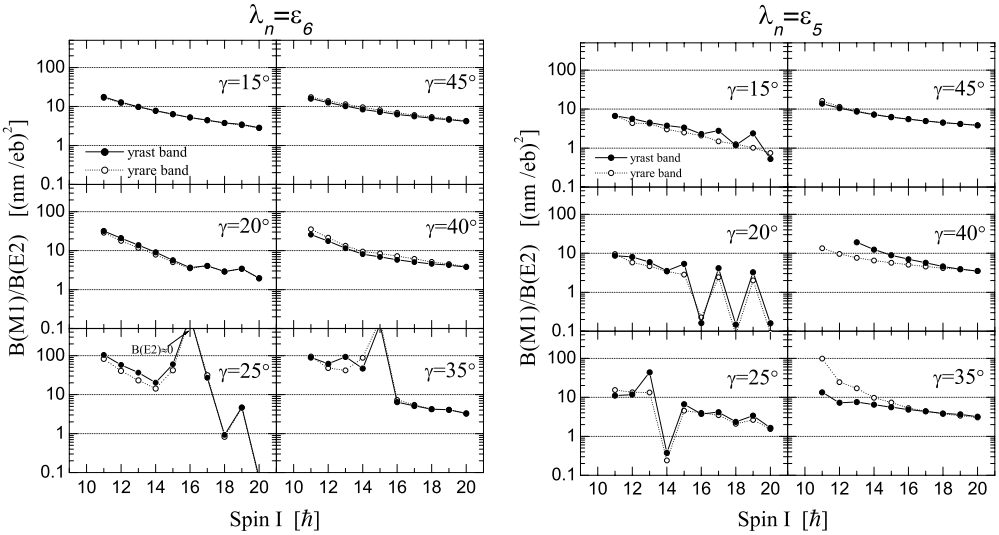

FIG. 6. Calculated $B(M1)/B(E2)$ values for the yrast and yrare bands. The same parameters as Fig. 3 are used; $\lambda_n = \varepsilon_6$ (left panel) and $\lambda_n = \varepsilon_5$ (right panel).

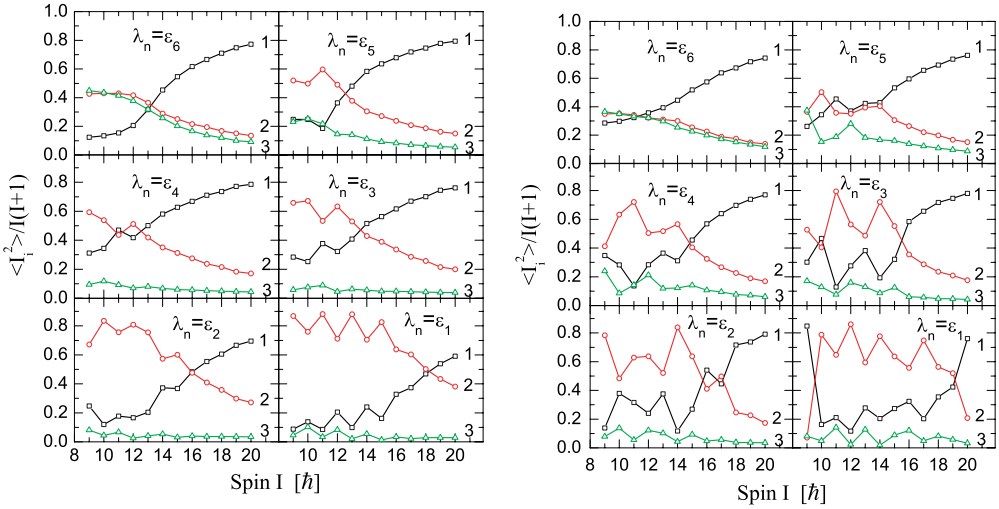

FIG. 7. (Color online) For the yrast and yrare bands, the average contribution of three components to the total angular momentum $\langle \hat{I}_i^2 \rangle / I(I+1)$, $i = 1, 2, 3$, in the intrinsic frame is plotted as a function of spin I. The same parameters as Fig. 2 are used. Open squares, open circles, and open triangles correspond to the 1-axis, 2-axis, and 3-axis, respectively.

For $\lambda_n = \varepsilon_6$, around $I = 13$, the contributions from the three directions are comparable for both yrast and yrare bands. This corresponds to a typical case of aplanar rotation. In fact, the contributions to the total angular momentum from all three directions are not negligible[2] in the spin interval $(9 < I < 20)$. Therefore the aplanar solution is realized for this spin interval and chiral doublet bands are expected. The statement is also true for the case $\lambda_n = \varepsilon_5$, with the exception that the contribution from the third component is a little smaller compared with the case $\lambda_n = \varepsilon_6$. As the Fermi energy surface λ_n decreases, the contribution from the third component becomes smaller, the total angular momentum will mainly lie in the 1–2 plane, and an aplanar rotation of the nucleus becomes a planar one. For both $\lambda_n = \varepsilon_4$ and ε_3, aplanar solutions can only be expected around $I \sim 11$. For $\lambda_n = \varepsilon_2$ and ε_1, there exist only planar rotations. In Fig. 7, there are some fluctuations of $\bar{I}_i^2/I(I+1)$ for $\lambda_n = \varepsilon_1, \varepsilon_2, \varepsilon_3$, and ε_4, owing to the strong interactions between different bands.

The expectation values $\bar{R}_i$ and $\bar{j}_{pi}, \bar{j}_{ni}$ have been investigated for $\lambda_n = \varepsilon_6, \ldots, \varepsilon_1$ as functions of the spin I. For simplicity, the cases for $\lambda_n = \varepsilon_6, \varepsilon_5$, and ε_1 are shown in Figs. 8, 9, and 10, respectively.

In Fig. 8, for $\lambda_n = \varepsilon_6$, similar to the results in Refs. [1,3], the collective angular momentum and valence-proton and valence-neutron angular momentum align along the intermediate axis (1-), the short axis (2-), and the long axis (3-), respectively. Since these three angular momenta are mutually perpendicular, a chiral picture results. In Fig. 9, for $\lambda_n = \varepsilon_5$, the configuration is similar to one proton plus three neutron holes in a single $h_{11/2}$ shell. In this case, the orientations of $\vec{R}$ and $\vec{j}_p$ are similar to those in Fig. 8, while the third component of the angular momentum $\vec{j}_n$ is reduced. The total angular momentum $\vec{I}$ is still aplanar, but its inclination angle to the 1–2 plane becomes smaller. As the neutron Fermi energy surface decreases, the hole-like odd neutron will switch to a particle-like one, and $\vec{j}_n$ will align from the 3-axis to the 2-axis. Then the valence proton and neutron both align to the 2-axis, with the collective angular momentum along the 1-axis, and together they give the total

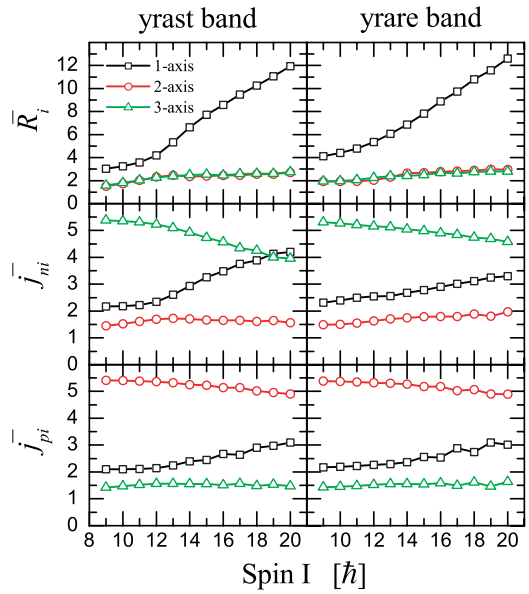

FIG. 8. (Color online) For the yrast and yrare bands, the expectation values for the three components of the collective, odd-neutron, and odd proton angular momenta—defined by $\bar{R}_i = \sqrt{\langle \hat{R}_i^2 \rangle}$, $\bar{j}_{pi} = \sqrt{\langle \hat{j}_{pi}^2 \rangle}$, and $\bar{j}_{ni} = \sqrt{\langle \hat{j}_{ni}^2 \rangle}$ $(i = 1, 2, 3)$—are plotted as functions of spin I. The same parameters as Fig. 2 are used, except that $\lambda_n = \varepsilon_6$. Open squares, open circles, and open triangles correspond to the 1-axis, 2-axis, and 3-axis, respectively.

[2]According to quantum physics, the minimum contribution from one direction to an angular momentum I is given by the value $\{\frac{1}{2}[I(I+1) - I^2]\}/I(I+1)$, when the angular momentum is perpendicular to this direction.

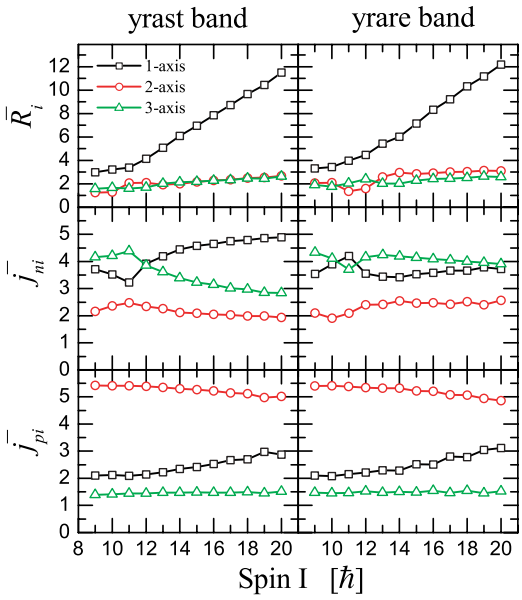

FIG. 9. (Color online) Same as Fig. 8, except that $\lambda_n = \varepsilon_5$.

angular momentum in the 1–2 plane. This is a planar solution shown in Fig. 10. Noted that in all cases the expectation values along the 1-axis for $\vec{j}_n$ and $\vec{j}_p$ increase with I because of the rotational alignment of odd particles.

The average core contribution to the total angular momentum can be seen in the upper panels of Figs. 8, 9, and 10. In Fig. 8, we note that the core contribution for the 14^+ state in both the yrast and the yrare bands ($R \sim 6.5\hbar$) is comparable with the contributions from the valence proton and valence neutron. The latter is consistent with the result in Ref. [46]. In Figs. 8 and 9, $\bar{R}_1$ increases by $8\hbar$ (from ~ 4 to $\sim 12\hbar$) as the spin I changes from $12\hbar$ to $20\hbar$. This demonstrates that the increase of the total angular momentum is mainly due to the collective rotation for $I \geqslant 12$. Therefore the transition

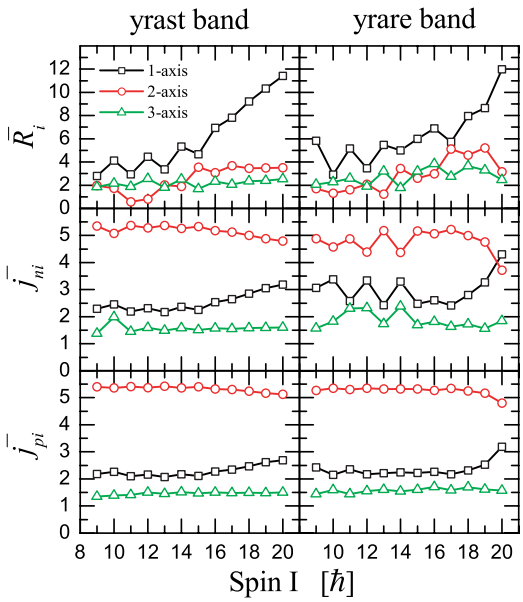

FIG. 10. (Color online) Same as Fig. 8, except that $\lambda_n = \varepsilon_1$.

probabilities $B(E2, I \rightarrow I-2)$ corresponding to the collective rotation should be large for $I \geqslant 14$. These results are consistent with the $B(E2)$ values discussed in Fig. 4. For the lower spin region near the bandhead ($I \leqslant 12$), the increase of I comes mainly from the contributions of the valence proton and neutron while the contribution from the core stays the same. For $\lambda_n = \varepsilon_1$ in Fig. 10, the collective angular momentum at low spin range $I < 16$ exhibits odd-even staggering, which is consistent with the energy spectrum in Fig. 1.

IV. CONCLUSION

A particle rotor model with a quasi-proton and a quasi-neutron coupled with a triaxial rotor is developed and applied to study chiral doublet bands with configurations of an $h_{11/2}$ proton and an $h_{11/2}$ quasi-neutron. With pairing correlations taken into account by the BCS method, a proton and many neutron holes coupled with a triaxial rotor can be simulated by changing the neutron Fermi level from the top $h_{11/2}$ orbit ε_6 to the lowest one ε_1.

The energy spectra, electromagnetic properties, as well as the orientations of the angular momenta of the doublet bands have been investigated in detail. The results are summarized as follows:

(i) Aplanar rotation exists at least for $\lambda_n = \varepsilon_6$ and $\lambda_n = \varepsilon_5$ in a certain spin interval. The contributions from the three axes are comparable to each other for the partner bands. This demonstrates that chiral geometry holds even for the valence nucleons deviating from a pure particle-hole configuration.

(ii) The near-constant energy separation (~200 keV) between the partner bands, which has been observed in many candidate chiral bands experimentally, has been obtained for $\lambda_n = \varepsilon_6$ and $\lambda_n = \varepsilon_5$ for certain spin and deformation γ intervals.

(iii) Either a deviation of the core shape from $\gamma = 30^\circ$ or a deviation of the Fermi energy surface from a particle-hole configuration will hinder the level degeneracy and prefer a near-constant energy difference.

(iv) For $15^\circ \leqslant \gamma \leqslant 45^\circ$, λ_n lies between ε_6 and ε_5, the $B(M1)/B(E2)$ values together with $B(E2)$ and $B(M1)$ values for the yrast bands are close to those in yrare bands, which may hold for all chiral bands.

(v) The odd-even staggering of $B(M1)/B(E2)$ values is strongly influenced by the deformation γ as well as the Fermi surface λ, which suggests that the odd-even staggering of $B(M1)/B(E2)$ values may not be a general feature for the chiral bands.

With pairing treated by the BCS approximation, the present quasiparticle PRM is aimed at simulating one proton and many neutron holes coupled with a triaxial rotor. After a detailed analysis of the angular momentum orientations, energy separation between the partner bands, and behavior of electromagnetic transitions, it is demonstrated that aplanar rotation, or equivalently chiral geometry, does exist beyond the simple one proton and one neutron hole coupled with a triaxial rotor. While simulating multiple valence particles here by adjusting the Fermi energy, one may argue that

the valence particles dumped into the BCS vacuum in the present model cannot contribute to the moments of inertia. However, as the main focus is the nuclei in the $A \geqslant 100$ mass region, the influence by such approximation should not result in a serious problem. Of course, a model with multi-proton particles (holes) and multi-neutron holes (particles) coupled explicitly with a triaxial rotor is necessary. Future work should also be devoted to replacing the present single-j shell by a more realistic single-particle potential, such as the Nilsson potential.

ACKNOWLEDGMENTS

The authors express their sincere gratitude to G. C. Hillhouse for helpful comments regarding this manuscript. This work is supported by the National Natural Science Foundation of China under Grant Nos. 10505002, 10435010, 10605001, and 10221003 and the Postdoctoral Science Foundation of China under Grant No. 20060390371.

[1] S. Frauendorf and J. Meng, Nucl. Phys. **A617**, 131 (1997).
[2] C. M. Petrache *et al*., Nucl. Phys. **A597**, 106 (1996).
[3] K. Starosta *et al*., Phys. Rev. Lett. **86**, 971 (2001).
[4] T. Koike, K. Starosta, C. J. Chiara, D. B. Fossan, and D. R. LaFosse, Phys. Rev. C **63**, 061304(R) (2001).
[5] A. A. Hecht *et al*., Phys. Rev. C **63**, 051302(R) (2001).
[6] D. J. Hartley *et al*., Phys. Rev. C **64**, 031304(R) (2001).
[7] R. A. Bark, *et al*., Nucl. Phys. **A691**, 577 (2001).
[8] X. F. Li *et al*., Chin. Phys. Lett. **19**, 1779 (2002).
[9] T. Koike, K. Starosta, C. J. Chiara, D. B. Fossan, and D. R. LaFosse, Phys. Rev. C **67**, 044319 (2003).
[10] G. Rainovski *et al*., Phys. Rev. C **68**, 024318 (2003).
[11] A. J. Simons *et al*., J. Phys. G **31**, 541 (2005).
[12] S. Y. Wang, Y. Z. Liu, T. Komatsubara, Y. J. Ma, and Y. H. Zhang, Phys. Rev. C **74**, 017302 (2006).
[13] C. Vaman, D. B. Fossan, T. Koike, K. Starosta, I. Y. Lee, and A. O. Macchiavelli, Phys. Rev. Lett. **92**, 032501 (2004).
[14] P. Joshi *et al*., Phys. Lett. **B595**, 135 (2004).
[15] P. Joshi *et al*., Eur. Phys. J. **A24**, 23 (2005).
[16] S. Zhu *et al*., Phys. Rev. Lett. **91**, 132501 (2003).
[17] J. A. Alcántara-Núñez *et al*., Phys. Rev. C **69**, 024317 (2004).
[18] J. Timár *et al*., Phys. Lett. **B598**, 178 (2004).
[19] J. Timár, C. Vaman, K. Starosta, D. B. Fossan, T. Koike, D. Sohler, I. Y. Lee, and A. O. Macchiavelli, Phys. Rev. C **73**, 011301(R) (2006).
[20] E. Mergel *et al*., Eur. Phys. J. A **15**, 417 (2002).
[21] V. I. Dimitrov, S. Frauendorf, and F. Dönau, Phys. Rev. Lett. **84**, 5732 (2000).
[22] V. I. Dimitrov, F. Dönau, and S. Frauendorf, Phys. Rev. C **62**, 024315 (2000).
[23] P. Olbratowski, J. Dobaczewski, J. Dudek, and W. Plóciennik, Phys. Rev. Lett. **93**, 052501 (2004).
[24] P. Olbratowski, J. Dobaczewski, and J. Dudek, Phys. Rev. C **73**, 054308 (2006).
[25] W. Koepf and P. Ring, Nucl. Phys. **A493**, 61 (1989).
[26] A. V. Afanasjev, P. Ring, and J. König, Nucl. Phys. **A676**, 196 (2000).
[27] H. Madokoro, J. Meng, M. Matsuzaki, and S. Yamaji, Phys. Rev. C **62**, 061301(R) (2000).
[28] J. Meng, J. Peng, S. Q. Zhang, and S.-G. Zhou, Phys. Rev. C **73**, 037303 (2006).
[29] S. Frauendorf, Rev. Mod. Phys. **73**, 463 (2001).
[30] J. Peng, J. Meng, and S. Q. Zhang, Phys. Rev. C **68**, 044324 (2003).
[31] J. Peng, J. Meng, and S. Q. Zhang, Chin. Phys. Lett. **20**, 1223 (2003).
[32] K. Starosta *et al*., Phys. Rev. C **65**, 044328 (2002).
[33] A. Klein, Phys. Rev. C **63**, 014316 (2000), and references therein.
[34] T. Koike, K. Starosta, and I. Hamamoto, Phys. Rev. Lett. **93**, 172502 (2004).
[35] T. Koike *et al*., FNS2002, Berkeley, CA, 2002, AIP Conf. Proc. No. 656, edited by P. Fallon and R. Clark (AIP, Melville, New York, 2003), p. 160.
[36] C. M. Petrache, G. B. Hagemann, I. Hamamoto, and K. Starosta, Phys. Rev. Lett. **96**, 112502 (2006).
[37] S. Y. Wang, S. Q. Zhang, B. Qi, and J. Meng, Chin. Phys. Lett. **24**, 664 (2007).
[38] D. Tonev *et al*., Phys. Rev. Lett. **96**, 052501 (2006).
[39] E. Grodner *et al*., Phys. Rev. Lett. **97**, 172501 (2006).
[40] S. Y. Wang, S. Q. Zhang, B. Qi, and J. Meng, Phys. Rev. C **75**, 024309 (2007).
[41] A. Bohr and B. Mottelson, *Nuclear Structure*, Vol. 2 (Benjamin, New York, 1975).
[42] P. Ring and P. Shuck, *The Nuclear Many-body Problem* (Springer-Verlag, New York, 1981), p. 107.
[43] J. Meyer-ter-vehn, Nucl. Phys. **A249**, 111 (1975).
[44] S. E. Larsson, G. Leander, and I. Ragnarsson Nucl. Phys. **A307**, 189 (1978).
[45] I. Ragnarsson and P. B. Semmes, Hyperfine Interact. **43**, 425 (1988).
[46] K. Starosta, T. Koike, C. J. Chiara, D. B. Fossan, and D. R. LaFosse, Nucl. Phys. **A682**, 375c (2001).